J Mater Sci: Mater Electron (2021) 32:23825–23833

Phase transition mechanism and application of silicon-doped VO_2 thin films to smart windows

Zhaorui Zou[1], Zhenhua Zhang[1], Jing Xu[1], Guoqiang Li[1], Rui Xiong[1], Yong Liu[1], and Jing Shi[1,*]

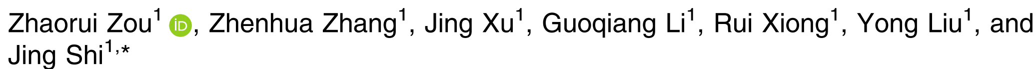

[1] *School of Physics and Technology, and the Key Laboratory of Artificial Micro/Nano Structures of Ministry of Education, Wuhan University, Wuhan 430072, China*

Received: 10 May 2021
Accepted: 1 August 2021
Published online:
2 September 2021

© The Author(s), under exclusive licence to Springer Science+Business Media, LLC, part of Springer Nature 2021

ABSTRACT

It is important to examine the mechanism of the metal–insulator transition (MIT) of vanadium dioxide (VO_2), which is of great significance, to understand the considerably related properties required for developing smart window applications. Here, we investigated the effect of the MIT on the thermochromic performance of VO_2. We prepared Si-doped VO_2 thin films and then used the sol–gel approach to deposit these thin films on Al_2O_3. X-ray diffraction (XRD) results showed that there was a metastable phase M2 in the VO_2 film, which is classified as a Mott insulator owing to electron correlation between the undimerized V ions. Additionally, we found that 3% Si-doped VO_2 thin films exhibited good thermochromic performance with a luminous transmittance (ΔT_{lum}) of 54.7% and a sol modulation efficiency (ΔT_{sol}) of 13.9%, which is superior to that of undoped VO_2 films with ΔT_{lum} of 37.2% and ΔT_{sol} of 7.3%. This can be attributed to simultaneous control of the transmittance in the visible and near-infrared regions of Si-doped VO_2 thin films. Therefore, this study provides a novel method of tuning the optical and electrical characteristics of VO_2 thin films.

1 Introduction

As a strongly correlated material, vanadium dioxide (VO_2) can undergo a first-order phase transformation at $\sim$ 340 K and has a reversible structural phase transformation from the M1 phase with low temperature to the R phase with high temperature [1–3]. For the M1 phase, the structural feature of VO_2 is a zigzag-type chain comprising V-atom dimers twisting down the R structure's c-axis (c_R). This will cause abrupt decrease in optical transmittance and electrical resistivity of multiple orders of magnitude in the event of metal–insulator transition (MIT) [4, 5]. These unique characteristics make VO_2 a potential material for various applications, such as smart windows [6], Mott transistors [2], sensors [7], and memory devices [8]. The mechanism of the MIT in VO_2 is not conclusive; it has been suggested that there are three major mechanisms. The first mechanism is a structure-driven Peierls transition explained by the

Address correspondence to E-mail: jshi@whu.edu.cn

https://doi.org/10.1007/s10854-021-06752-2

formation of V–V dimers along the rutile c_R below the phase transition temperature (T_c). The second mechanism is an electron-correlation-driven Mott transition. The third mechanism is a combination of the Peierls and Mott transitions. Many studies have shown that there is another low temperature metastable M2 phase (C2/m) that is closely related to VO_2 between the M1 and R phases [9, 10]. According to a previous study [11], the structure of the Mott insulation in the M2 phase is similar to that in the M1 phase, except that half of the V atoms continue to show dimerization in c_R, while the remaining half form a zigzag-type chain with equal spacing and a local moment of Heisenberg 1/2 spin.

VO_2 thin films have not been used in any recent practical applications of smart windows owing to three major challenges: low sol modulation efficiency (ΔT_{sol}) (< 10%), low luminous transmittance (ΔT_{lum}) (< 60%), and high T_c. Several attempts have been made to control T_c and improve the optical performance of VO_2 thin films using doping elements [12–15], designing multilayer structures [16–19], and forming composite films [20]. For example, 2.93% F-doped VO_2 nanoparticles can decrease the T_c to 35 °C and increase ΔT_{sol} to 10.7%, which can meet the requirements of reducing T_c and improving the thermochromic performance [13]. Mg-doped VO_2 leads to a wide bandgap, reducing T_c to 35 °C and improving ΔT_{sol} and ΔT_{lum} [16]. A buffer layer of TiO_2 films can increase T_c to 64 °C, with T_{lum} and ΔT_{sol} values of 53% and 5.2%, respectively [18]. Controlling the elemental doping ratio of VO_2 thin films is an effective method to change T_c, ΔT_{sol} and ΔT_{lum}.

Si-doped VO_2 films have been studied; however, the effect of Si dopants on the MIT is not clear and the optical properties of such films have not been greatly improved. For example, Wu et al. [21] observed that T_c was first adjusted to a low temperature and then irregularly transited to a high temperature in some Si-doped VO_2 films. Krammer et al. [22] reported that Si-doping increases T_c (an increase of $\sim$ 4.5 °C was reached). Meanwhile, Wu et al. [23] showed that Si-doped VO_2 films increased T_{lum} to 36.1% and ΔT_{sol} to 9.2% and decreased T_c to 46.1 °C. Therefore, it is necessary to experimentally explain the effects of Si dopants on the MIT and optical properties of VO_2 thin films.

In this study, we grew undoped and Si-doped VO_2 thin films on Al_2O_3 substrates using the sol–gel method. We systematically analyzed the crystal structure, electrical transport, and optical properties of these films. The results showed that a certain amount of Si-doping improves the optical properties, which considerably affects the practical applications of VO_2 thin films in smart windows.

2 Experimental details

In this study, we successfully prepared Si-doped VO_2 films at different Si concentrations on Al_2O_3 substrates using the sol–gel method. First, 0.67 g of $VO(acac)_2$ and SiO_2 powders of different concentrations were added to 20 mL of anhydrous methanol, and then, the solution was stirred for 5 min using a magnetic stirrer. Thereafter, we added 3.5 mL of hydrochloric acid (pH = 1) to the solution. Finally, 0.71 g of polyvinylpyrrolidone was added to the solution to form a sol. The concentration of SiO_2 [$SiO_2/VO(acac)_2 + SiO_2$] varied in the range of 0%, 1%, 3%, 5%, 8% and 10%, respectively. Before preparing the films, we conducted ultrasonic cleaning of the Al_2O_3 substrates two times for 15 min using acetone, deionized water, and anhydrous ethanol. The prepared sols were coated onto the Al_2O_3 substrates using a spinning coater at 3000 rpm for 15 s. The samples were first heated in an oven at 80 °C for 10 min and then annealed in a tubular furnace at 550 °C under Ar atmosphere.

X-ray diffraction (XRD, Rigaku Smartlab SE X-ray diffractometer) was conducted to analyze the crystal structures of VO_2 thin films. X-ray photoelectron spectroscopy (XPS, Escalab 250Xi) was used to determine the elemental compositions of all the thin films in the experiment using an Mg Kα X-ray source with a resolution of 0.45 eV under ultrahigh vacuum conditions. We investigated each thin film for its electrical transport characteristics using four-point probe modules in the physical property measurement system (Quantum Design PPMS-9). In addition, an ultraviolet–visible spectrophotometer (UV–Vis, CARY5000, Varian) with an additional heating module was used to measure the optical characteristics of all of the VO_2 films.

The wavelength ranges of T_{lum} and T_{sol} are between 380–780 nm and 300–2500 nm, respectively. The T_{sol} and T_{lum} values of all the VO_2 thin films can be calculated using the following integral formula: $T_i = \int \Phi_i(\lambda)T(\lambda)d\lambda / \int \Phi_i(\lambda)d\lambda$. Here, $T(\lambda)$ is the film

transmittance under the λ wavelength, i represents sol or lum, Φ_{sol} is the solar irradiance spectrum at 1.5 air mass, and Φ_{lum} is the standard luminous efficiency function (i.e., when the Sun is located 37° above the horizon). ΔT_{sol} and the near-infrared switching efficiency ($\Delta T_{2000\ nm}$) are obtained such that $\Delta T = T(T < T_c) - T(T < T_c)$. The formula of ΔT_{lum} can be expressed as follows: $\Delta T_{lum} = (T_{lum}(T < T_c) + T_{lum}(T < T_c))/2$.

3 Results and discussion

Figure 1 shows the typical XRD measurement of the Si-doped VO_2 crystalline film structures deposited on the Al_2O_3 substrates. We used a simple substrate, Al_2O_3, to facilitate the testing of the optical properties. Only three major diffraction peaks were observed for the VO_2 films, with ~ 27.8° corresponding to VO_2 M1 (011) and the other two peaks at ~ 37.6° and 41.8° corresponding to Al_2O_3 (0001) Kβ and Al_2O_3 (0001) Kα, respectively. Figure 1b shows the magnified view of Fig. 1a, illustrating that the diffraction peaks migrated to larger diffraction angles as the Si-doping concentration increased. The average grain size of crystal faces of the thin films can be determined using the Scherer equation: $D = K\lambda/B\cos\theta$. Here λ, K, θ, and B represent the XRD wavelength (0.1541 nm), Scherrer constant (0.89), diffraction angle, and full width at half-maximum, respectively. Using this formula, the average particle size reduction of the Si-doped films can be calculated (Table 1). This phenomenon may be attributable to the disorder in the VO_2 crystal lattice, indicating that Si-doping increases the number of nucleation centers [24]. The lattice parameter (d-spacing) was calculated

Table 1 Diffraction angle, interplanar crystal spacing and average grain diameter of (011) crystal plane of Si-doped VO_2 thin films

Sample (%)	2θ (011)	d-spacing/nm	D(011)/nm data ± err
0	27.81°	0.3205	18.47
1	27.84°	0.3201	17.64
3	27.89°	0.3195	17.60
5	27.98°	0.3185	17.19
8	28.04°	0.3178	16.80
10	28.13°	0.3168	13.26

using the Bragg equation: $2d\sin\theta = n\lambda$. Here, θ represents the diffraction angle, n is an integer, and λ is the wavelength. According to the calculations, the d-spacing decreased from 0.3168 nm for an undoped film to 0.3205 nm for a film with 10% Si-doping. This phenomenon may occur because Si^{4+} (0.04 nm) has a slightly smaller radius than V^{4+} (0.058 nm). Additionally, the reduction in the d-spacing may indicate the presence of in-plane tensile stress [25].

Figure 2 shows the XRD patterns for the undoped and 3% Si-doped VO_2 films at various temperatures. Examining the XRD patterns at various temperatures enables a further investigation of the structural changes associated with MIT, which is an effective way to observe accurate nanoscale alterations in the lattice structure. All samples were allowed to stabilize for 2 min at each temperature, followed by the measurement of the XRD patterns under the constant temperature in 0.1 °C. In Fig. 2a1, two diffraction peaks were observed at 27.8° and 27.7° associated with the M1 phase (011) and R phase (110) planes, respectively. Apart from the traditional major peak shift from M1(011) to R(110), another diffraction peak appeared at 28.25° associated with M2 (201) at the temperatures of 35–84 °C. When the temperature increased to 87 °C, the predominant R phase was

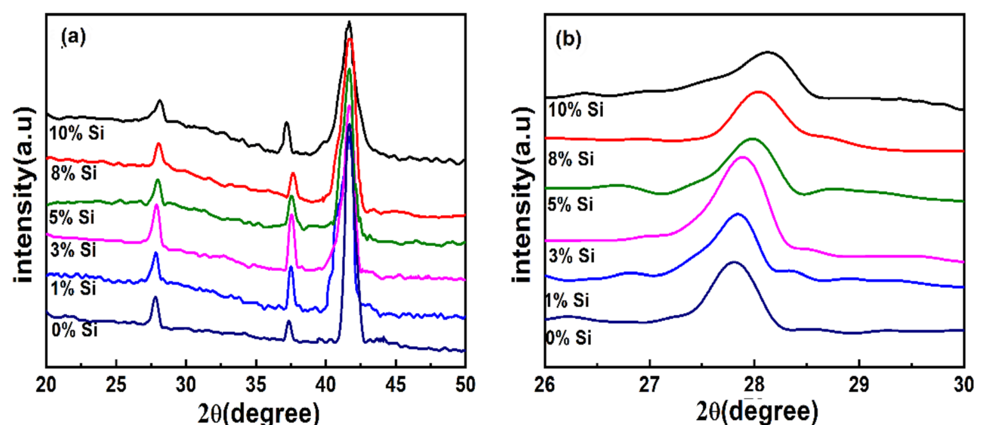

Fig. 1 **a**, **b** XRD patterns for the Si-doped VO_2 films in logarithmic coordinates

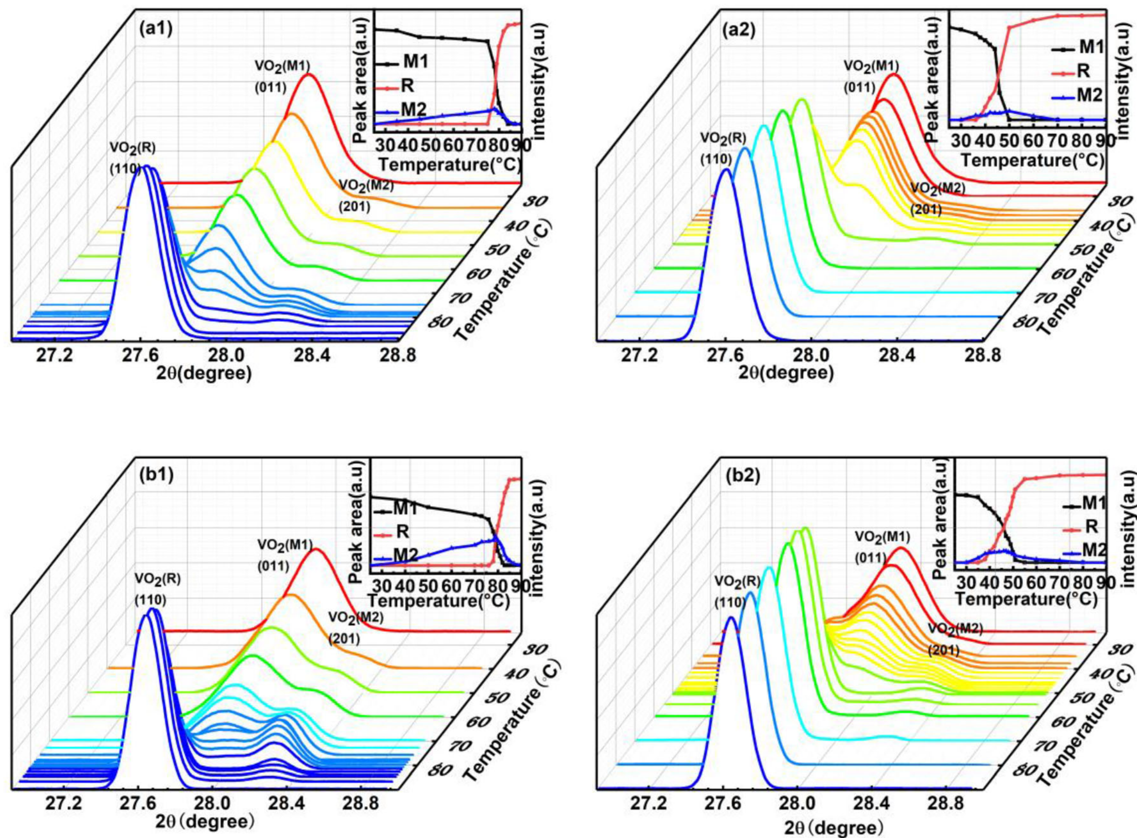

Fig. 2 XRD patterns for **a** undoped and **b** 3% Si-doped VO_2 films: **a1** and **b1** show the heating stages and **a2** and **b2** show the cooling stages. The change in the peak integral intensity with temperature is shown in the inset, with the M1 phase in black, the M2 phase in blue, and the R phase in red

observed and the M2 phase disappeared. Figure 2a2 shows the cooling XRD patterns for the undoped VO_2 films. The XRD patterns in inset show T_c at 78.3 °C and 45.1 °C in the heating and cooling stages, respectively. Figure 2b1 shows that the M2 phase can be observed when the temperature increases to 60 °C after 3% Si-doping. As the temperature increases to 90 °C, the R phase begins to dominate and the M2 phase gradually disappears. Figure 2b2 shows that, after 3% Si-doping, the M2 phase can be clearly observed when the temperature drops to 70 °C in the cooling phase test. As the temperature drops to 30 °C, the M1 phase begins to dominate and the M2 phase gradually disappears. The XRD patterns in the inset of Figs. 2b1 and b2 show T_c at 79 °C and 45.9 °C in the heating and cooling stages, respectively.

To analyze the valence states of the V and O atoms on the surface of the Si-doped VO_2 films, we acquired the V 2p and O 1s core-level XPS spectra (Fig. 3). The C 1s peak (284.6 eV) was used to correct the positive charge effect-induced shift. The core-level binding energy of the O 1s peak can be deconvoluted into two peaks located at ~ 530.2 and 531.5 eV assigned to the V–O [25] and Si–O bonds [26], respectively. The V $2p_{1/2}$ and V $2p_{3/2}$ peaks were observed at 523.5 and 515.9 eV, respectively, because of the V 2p spin–orbit splitting. The binding energy difference is 14.3 eV comparing O 1s with V $2p_{3/2}$, which conformed to the 14.0 eV value for VO_2 nanoparticles, indicating that V^{4+} was the major valence state in the Si-doped VO_2 films [27]. The V $2p_{3/2}$ peak can decompose into two peaks located near 515.9 and 517.3 eV, corresponding to V^{4+} and V^{5+} ions, respectively. In addition, the O/V ratio can be estimated from the integrated area of the empirical formula, $(2I_V{}^{4+} + 2.5I_V{}^{5+})/(I_V{}^{4+} + I_V{}^{5+})$ [25], indicating the near stoichiometry O/V ratio inside the prepared VO_2 films. It was inferred that the O/V ratios were 2, 2.23, 2.31, 2.40 and 2.41 when the Si concentration was increased to 1%, 3%, 5%, 8% and 10%, respectively. The XPS data analysis indicated that the chemical state of the Si-doped V changed from V^{4+} to V^{5+} and

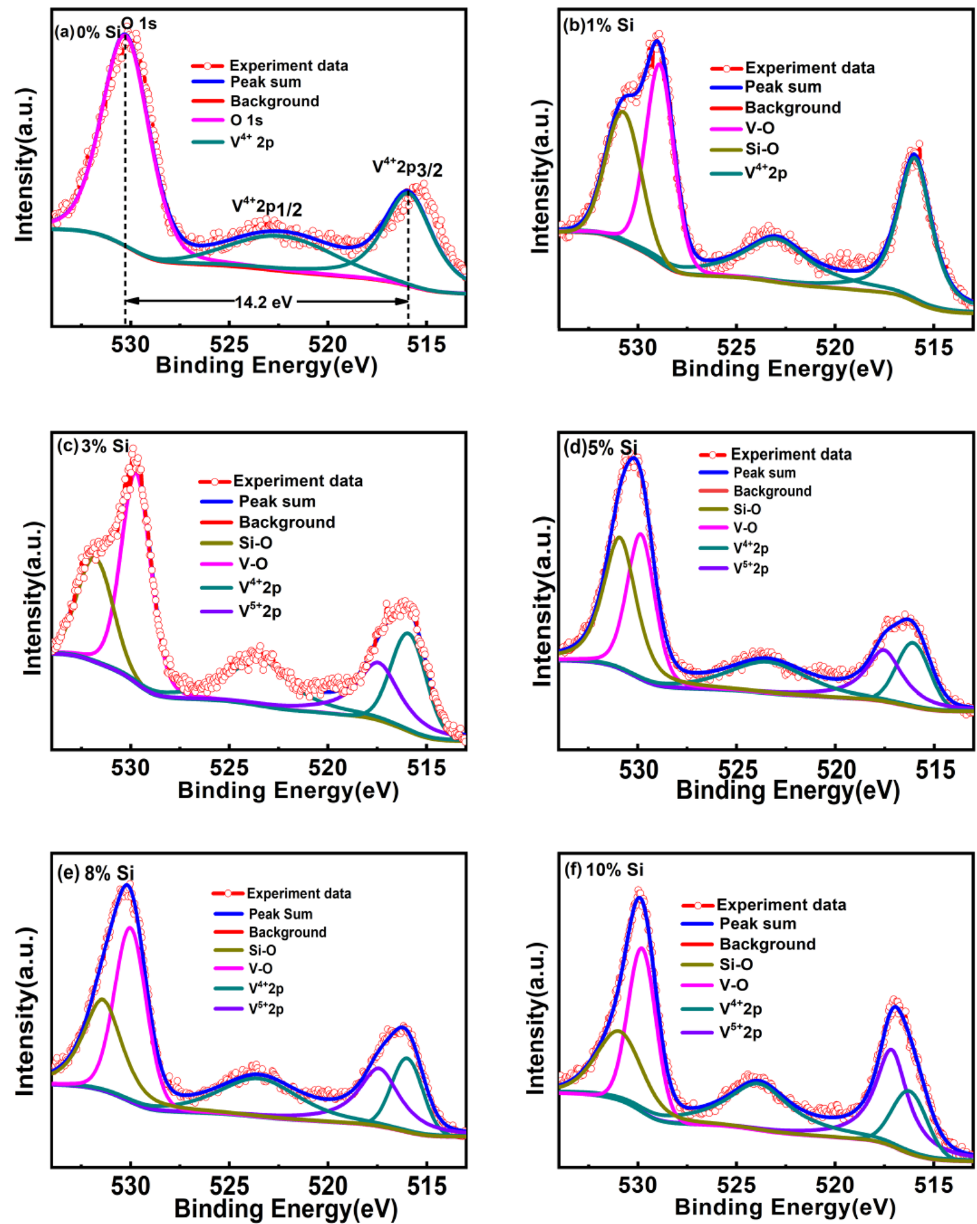

Fig. 3 V 2p and O 1s core-level XPS spectra for the Si-doped VO_2 samples

V^{4+}, enhancing the electron–electron correlation and therefore increasing the peak area of the M2 phase [9, 28].

To investigate the electrical transport characteristics in VO_2 samples doped with different Si concentrations, we measured the resistances of all the samples as the function of temperature using the PPMS (Fig. 4). The heating and cooling curves of all the samples were fitted using Gaussian functions to further determine the T_c, thermal hysteresis (ΔH), and transition sharpness (ΔT) of the Si-doped VO_2 thin films. The minimum value of the Gaussian function was the transition temperatures of $T_{heating}$ and $T_{cooling}$, that is, the relationship curve between dR/dT and the temperature, as shown in the various illustrations in Fig. 4. T_c and ΔH were determined using the following equations: $T_c = (T_{heating} + T_{cooling})/2$ and $\Delta H = T_{heating} - T_{cooling}$, respectively. Similar to previous reports, T_c increased slightly with increasing Si concentration [22]. As shown in Table 2, the T_c values for the 0%, 1%, 3%, 5%, 8% and 10% Si-doped VO_2 films are 333.9, 335.9, 336.1, 336.8, 337.0 and 341.1 K, respectively. In the Si-doped VO_2 films, the small particle radius of Si^{4+} replaces the large particle radius of V^{4+}, leading to lattice distortion. The lattice distortion affects the interactions between

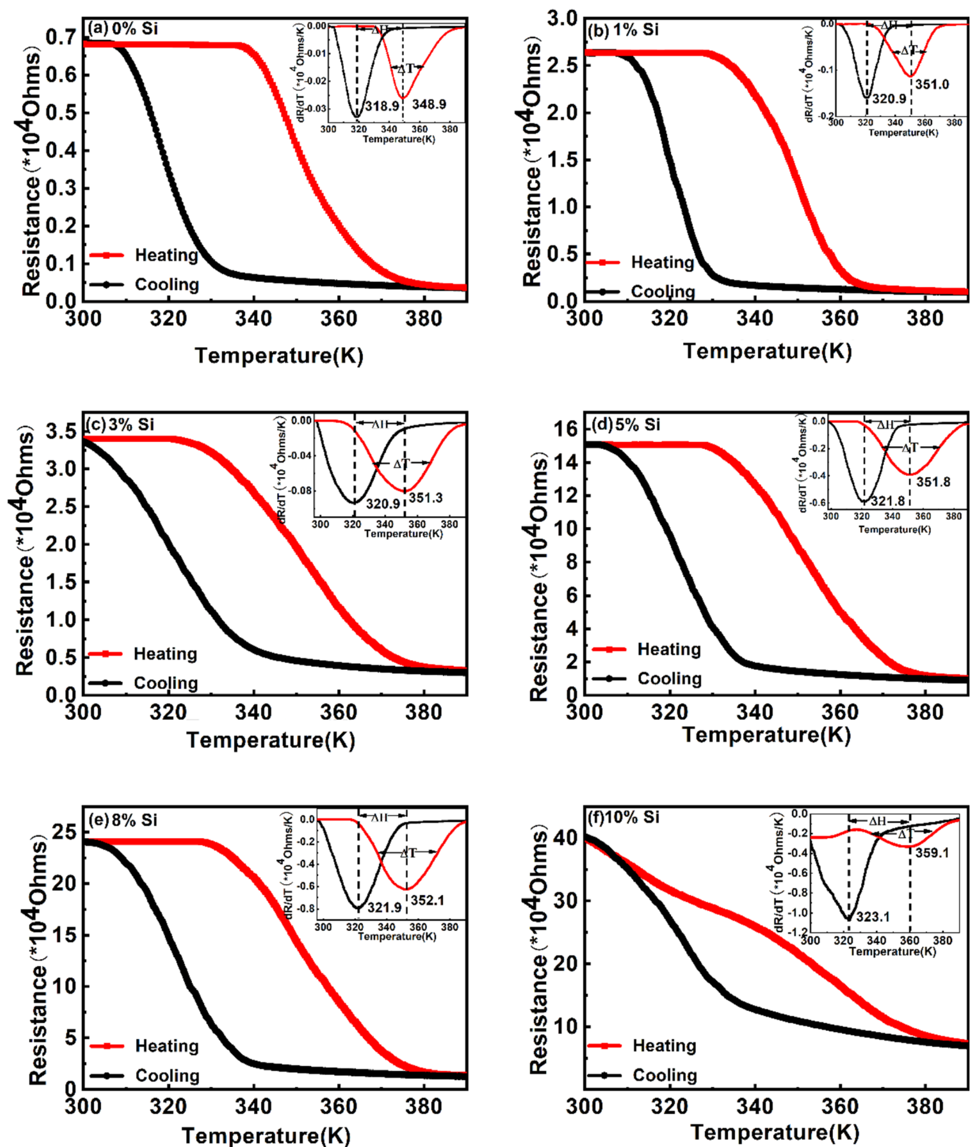

Fig. 4 Thermal hysteresis resistance loops of the Si-doped VO_2 samples. Insets show the rate of change of the resistance as a function of temperature

Table 2 $T_{heating}$, $T_{cooling}$, T_c, ΔT and ΔH of Si-doped VO_2 samples

Sample (%)	$T_{heating}$ (K)	$T_{cooling}$ (K)	T_c (K)	ΔH (K)	ΔT (K)
0	348.9	318.9	333.9	30.0	20.7
1	351.0	320.9	335.9	30.1	22.0
3	351.3	320.9	336.1	30.4	33.9
5	351.8	321.8	336.8	30.0	36.6
8	352.1	321.9	337.0	30.2	37.7
10	359.1	323.1	341.1	36.0	38.5

the V 3d and O 2p orbitals, especially the $d_{//}$ and π^* electronic orbital occupancy [29]. With an increase in the Si-doping concentration, the π^* band shifts upward and the π^* orbital electron occupancy decreases, increasing T_c and the insulator resistance [30]. The 10% Si-doped VO_2 films show a much wider ΔH of 36.0 K compared with the undoped VO_2 films. The increase in ΔH with Si-doping may be due to the additional defects or scattered strain in the VO_2 crystal lattice [31]. Finally, increasing the Si-doping concentration from0%, 1%, 3%, 5%, 8% and 10% increases ΔT from 20.7 K to 22.0, 33.9, 36.6, 37.7 and

38.5 K, respectively. The obvious phase transition hysteretic degradation may be due to the presence of Si ions in the VO_2 lattice, which leads to the conjugate effect on the V–V chain and a V–O bond adjustment at the same time, limiting the MIT characteristics of the VO_2 films. In addition, the increase in ΔT may be explained by the crystal showing a difference in T_c. The transition in the polycrystalline films is reflected by the distribution of different crystal T_c values. The change in T_c in a single crystal may be caused by strain. The lattice disorder, number of defects, and grain boundary density of doped films are better than those of undoped VO_2 films.

Figure 5a shows the optical transmittance $T(\lambda)$ at the wavelengths in the range of 300–2500 nm for the Si-doped VO_2 thin films between 30 °C (solid curves) and 90 °C (dotted curves). The yellow shaded area indicates the standard solar spectrum. It can be seen that for each film, the transmittance decreased at 90 °C compared with its transmittance at 30 °C, suggesting that all the films have good thermochromic properties. Figure 5b shows ΔT_{lum}, ΔT_{sol} and ΔT_{2000nm} for all the samples. When the Si-doping concentration increased to 3%, ΔT_{sol} increased significantly from 7.3% to 13.9%. ΔT_{lum}, ΔT_{sol} and ΔT_{2000nm} first increased and then decreased with increasing Si-doping content. When the Si-doping content reached 3%, the ΔT_{sol}, ΔT_{lum} and ΔT_{2000nm} values were 13.9%, 54.7% and 45.4%, respectively. In addition, the bandgap values were 1.58, 1.93, 2.02, 1.86, 1.85 and 1.81 eV, corresponding to 0%, 1%, 3%, 5%, 8% and 10%, respectively. The bandgap increased with increasing Si-doping concentration, leading to higher barrier energy for the film and ultimately increasing T_c [32].

The VO_2 phase transformation is a complicated process, and its driving mechanisms, in addition to temperature, could include electric current, electric field, and optical radiation. Therefore, the mechanism of the phase change has been debated and several different theories have been invoked, including lattice symmetry drive, the Peierls transition, and the Mott transition theories. In early 1968, Mott et al. [33] proposed that the phase transition of VO_2 was caused by electronic interactions. However, they did not explicitly prove this theory. Kim et al. [34] conducted an XRD test of the VO_2 MIT separation of phase and SPT transitions and confirmed the existence of the M_2 phases, such as the monoclinic metallic phase or the strong metallic phase. Therefore, the M1 → M2 → R phase transition process has been confirmed for VO_2 and the phase transition occurs prior to the transformation of the M phase into the R phase. However, the crystal structure does not change. From Figs. 2 and 4, the M2 phase generated in the MIT process of VO_2 implies that SPT occurs later; therefore, the

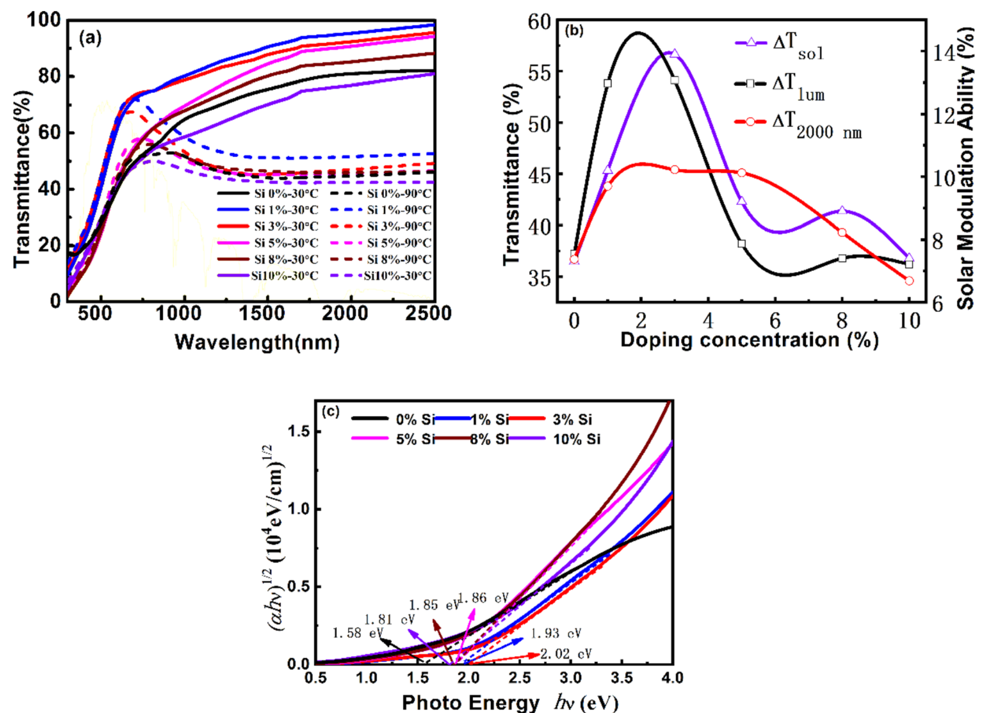

Fig. 5 **a** Optical transmittance spectra for Si-doped VO_2 samples between 30 °C and 90 °C. **b** ΔT_{lum}, ΔT_{sol} and ΔT_{2000nm} of the Si-doped VO_2 samples. **c** Bandgap of the Si-doped VO_2 samples at 30 °C

phase transition of VO_2 belongs to the Mott transition. The electron transition Mott criterion is $(n_c)^{1/3}a_B \approx 0.25$, where a_B is the effective Bohr radius and n_c is the critical density. From the formula, the n_c values of the undoped and Si-doped VO_2 films were $n_c \approx 3 \times 10^{18}$ cm^{-3} and $n_c \approx 4.3 \times 10^{18}$ cm^{-3}, respectively. The n_c value had the same order of magnitude as the VO_2 electron density under the phase transformation point, $n_c \approx 10^{18} - 10^{19}$ cm^{-3} [35]. The results confirmed that in VO_2, MIT was a pure electronic Mott–Hubbard transformation.

The following aspects of the change in T_c and the optical performances due to Si^{4+} doping have been resolved. First, Wu [36] reported that the modulated T_c and optical properties are attributable to lattice distortion and electronic effects. Second, Si-doped VO_2 films have an increased bandgap because of the decrease in their π^* orbital electron occupancy. The decrease in the shielding strength for the strong electron–electron correlations in the $d_{//}$ orbital increases T_c, which is consistent with previously reported results for Ti-doped VO_2 films [30]. Sun et al. [37] reported that the change in T_c can be attributed to the grain size effect. Therefore, the XRD results in Fig. 1 indicate that Si^{4+} ions replace V^{4+} in the VO_2 lattice, decrease the grain size, and increase the nucleation centers, resulting in a lattice distortion in the VO_2 films. Therefore, the Si^{4+} ion-doping affects T_c and the optical properties. Finally, the change in T_c may be due to strain [27]. Doping with Si^{4+} ions resulted in a gradual decrease of the d-spacing in the VO_2 films, indicating the existence of in-plane tensile stress and significantly improving VO_2 films for use in smart windows.

4 Conclusions

In this study, Si-doped VO_2 samples with different Si concentrations were synthesized using the sol–gel approach. The structure and thermochromic properties of all the samples were characterized using various techniques. The results showed that with an increase in the Si-doping content, the optical characteristics can be improved with a slight increase in T_c. The T_c values for the undoped and 3% Si-doped VO_2 samples were 333.9 K and 336.1 K, ΔT_{sol} were 7.3% and 13.9%, ΔT_{lum} were 37.2% and 54.7%, and ΔT_{2000nm} were 36.7% and 45.4%, respectively. Si-doping enhanced the strong electron–electron correlation of the $d_{//}$ orbitals, thus increasing T_c. In addition, the M2 phase was insulated by the Mott transition within the VO_2 thin films at an intermediate temperature for the phase transition, verifying the role of potent electron–electron correlations in driving MIT. This study shows that Si-doped VO_2 thin films can be prepared to slightly increase T_c, simultaneously improving ΔT_{lum}, ΔT_{2000nm} and ΔT_{sol}.

Acknowledgements

This work was supported by the National Natural Science Foundation of China 12074291, 11804211, 11905119.

References

1. S. Zhang, I.S. Kim, L.J. Lauhon, Nano Lett. **11**, 1443–1447 (2011)
2. M.M. Qazilbash, M. Brehm, B.G. Chae, P.-C. Ho, G.O. Andreev, B.J. Kim, S.J. Yun, A.V. Balatsky, M.B. Maple, F. Keilmann, H.T. Kim, D.N. Basov, Science **318**, 1750–1753 (2007)
3. Z. Shao, X. Cao, Q. Zhang, S. Long, T. Chang, F. Xu, Y. Yang, P. Jin, Sol. Energy Mater. Sol. Cells. **200**, 110044 (2019)
4. R. Zhang, C. Yin, Q. Fu, C. Li, G. Qian, X. Chen, C. Lu, S. Yuan, X. Zhao, H. Tao, Ceram. Int. **44**, 2809–2813 (2018)
5. I. Top, R. Binions, C. Sol, I. Papakonstantinou, M. Holdynski, S. Gaiaschi, I. Abrahams, J. Mater. Chem. C **6**, 12555–12565 (2018)
6. J. Jin, D. Zhang, X. Qin, H.I.A. Imran, P. Fan, Energy Build. **202**, 109345 (2019)
7. C.M. Leroy, M.F. Achard, O. Babot, N. Steunou, P. Masse, J.L. Binet, N. Brun, R. Backov, Chem. Mater. **19**, 3988–3999 (2017)
8. T. Driscoll, H.T. Kim, B.G. Chae, B.J. Kim, Y.W. Lee, N.M. Jokerst, S. Palit, D.R. Smith, M.D. Ventra, D.N. Basov, Science **325**, 1518 (2009)
9. D. Lee, T. Min, G. Lee, J. Kim, S. Song, J. Lee, J. Bae, H. Kang, J. Lee, S. Park, J. Phys. Chem. Lett. **11**, 9680–9688 (2020)
10. A. Tselev, I.A. Luk'yanchuk, I.N. Ivanov, J.D. Budai, J.Z. Tischler, E. Strelcov, A. Kolmakov, V. Kalinin, Nano Lett. **10**, 4409 (2010)
11. J.P. Pouget, H. Launois, J.P. D'Haenens, P. Merenda, T.M. Rice, Phys. Rev. Lett. **13**, 873 (1975)
12. L. Dai, S. Chen, J. Liu, Y. Gao, J. Zhou, Z. Chen, Phys. Chem. Chem. Phys. **15**(28), 11723–11729 (2013)

13. C. Chen, Y. Zhao, X. Pan, V. Kuryatkov, A. Bernussi, M. Holtz, Z. Fan, J. Appl. Phys. **110**, 023707 (2011)
14. Y. Xu, W. Huang, Q. Shi, Y. Zhang, L. Song, Y. Zhang, J. Sol-Gel. Sci. Technol. **64**(2), 493–499 (2012)
15. M. Panagopoulou, E. Gagaoudakis, N. Boukos, E. Aperathitis, G. Kiriakidis, D. Tsoukalas, Sol. Energy Mater Sol. Cells **157**, 1004–1010 (2016)
16. J. Zheng, S. Bao, P. Jin, Nano Energy **11**, 136–145 (2015)
17 N.R. Mlyuka, G.A. Niklasson, C.G. Granqvist, Sol. Energy Mater. Sol. Cells **93**(9), 1685–1687 (2009)
18. C. Kang, C. Zhang, L. Zhang, S. Liang, C. Geng, G. Cao, H. Zong, M. Li, Appl. Surf. Sci. **463**, 704–712 (2019)
19. V.R. Kolbunov, A.I. Ivon, Y.A. Kunitskiy, I.M. Chernenko, Ceram. Int. **39**(4), 3613–3620 (2013)
20. F. Xu, X. Cao, J. Zhu, G. Sun, R. Li, S. Long, H. Luo, P. Jin, Mater. Lett. **222**, 62–65 (2018)
21. X. Wu, Z. Wu, Z. Liu, C. Ji, Z. Huang, Y. Su, J. Gou, J. Wang, Y. Jiang, Appl. Phys. Lett. **109**, 111903 (2016)
22. A. Krammer, O. Bouvard, A. Schüler, Energy Procedia **122**, 745–750 (2017)
23. X. Wu, Z. Wu, H. Zhang, R. Niu, Q. He, C. Ji, J. Wang, Y. Jiang, Surf. Coat. Technol. **276**, 248–253 (2015)
24. J. Du, Y. Gao, H. Luo, L. Kang, Z. Zhang, Z. Chen, C. Cao, Sol. Energy Mater. Sol. Cells **95**(2), 469–475 (2011)
25. M. Wang, L. Fan, J. Bian, D. Zhang, H. Liu, H. Sun, Y. Luo, J. Mater. Sci. Mater. Electron. **28**, 11046–11052 (2017)
26. M.M. Fadlelmula, E.C. Sürmeli, M. Ramezani, T.S. Kasırga, Nano Lett. **17**, 1762–1767 (2017)
27. N. Shen, S. Chen, Z. Chen, X. Liu, C. Cao, B. Dong, H. Luo, J. Liu, Y. Gao, J. Mater. Chem. A **2**, 15087 (2014)
28. S. Zhang, I.S. Kim, L.J. Lauhon, Nano Lett. **11**(4), 1443–1447 (2011)
29. R. Zhang, H. Jin, D. Guo, J. Zhang, Z. Zhao, Y. Zhao, J. Li, Ceram. Int. **42**, 18764–18770 (2016)
30. K. Huang, Y. Meng, X. Xu, P. Chen, A. Lu, H. Li, C. Wang, X. Chen, J. Phys. Condens. Matter **29**, 355402 (2017)
31. J. Jian, A. Chen, Y. Chen, X. Zhang, H. Wang, Appl. Phys. Lett. **111**, 153102 (2017)
32. Z. Zou, Z. Zhang, J. Xu, Z. Yu, M. Cheng, R. Xiong, Z. Lu, Y. Liu, J. Shi, J. Alloy. Comp. **806**, 310–315 (2019)
33. N.F. Mott, Rev. Mod. Phys. **40**(4), 677 (1968)
34. B.J. Kim, Y.W. Lee, S. Choi, J.W. Lim, S.J. Yun, H.T. Kim, Phys. Rev. B **77**, 235401 (2008)
35. G. Stefanovich, A. Pergament, D. Stefanovich, J. Phys.: Condens. Matter. **12**, 8837 (2000)
36. Y. Wu, Sci. Rep. **5**, 9328 (2015)
37. Y. Sun, S. Jiang, W. Bi, R. Long, X. Tan, C. Wu, S. Wei, Y. Xie, Nanoscale **3**, 4394 (2011)

Publisher's Note Springer Nature remains neutral with regard to jurisdictional claims in published maps and institutional affiliations.